
Inter-tropical African precipitation regime shifts dominated by tropical easterly jet

Received: 6 August 2025

Accepted: 22 December 2025

Cite this article as: Yao, S.-L., Wu, R., Lin, P. *et al.* Inter-tropical African precipitation regime shifts dominated by tropical easterly jet. *npj Clim Atmos Sci* (2025). <https://doi.org/10.1038/s41612-025-01312-5>

Shuai-Lei Yao, Renguang Wu, Pengfei Lin, Pao-Shin Chu, Haosu Tang & Pengfei Wang

We are providing an unedited version of this manuscript to give early access to its findings. Before final publication, the manuscript will undergo further editing. Please note there may be errors present which affect the content, and all legal disclaimers apply.

If this paper is publishing under a Transparent Peer Review model then Peer Review reports will publish with the final article.

Inter-tropical African precipitation regime shifts dominated by tropical easterly jet

Shuai-Lei Yao¹, Renguang Wu^{2*}, Pengfei Lin^{1,3*}, Pao-Shin Chu⁴, Haosu Tang⁵, Pengfei Wang¹

¹Key Laboratory of Earth System Numerical Modeling and Application, Institute of Atmospheric Physics, Chinese Academy of Sciences, Beijing 100029, China

²School of Earth Sciences, Zhejiang University, Hangzhou 310058, China

³College of Earth and Planetary Sciences, University of Chinese Academy of Sciences, Beijing 100049, China

⁴Department of Atmospheric Sciences, School of Ocean and Earth Science and Technology, University of Hawai'i at Mānoa, HI 96822, USA

⁵School of Geography and Planning, University of Sheffield, Sheffield, UK

Corresponding authors: renguang@zju.edu.cn; linpf@mail.iap.ac.cn

Abstract

Since the 1990s, inter-tropical Africa (ITA) has experienced consecutive calamitous droughts during the boreal spring. Although the observed precipitation regime changes have been attributed to tropical Indian Ocean-western Pacific warming and/or tropical Pacific La Niña-like cooling, the model-projected past-to-future widespread wetting response to anthropogenic warming overshadows qualitative attributions of decadal shifts in historical precipitation regimes and the reliability of near-term projections. The causes of ITA precipitation regime shifts and the likelihood of their future continuation remain unclear. Here, we reveal that the observed monopolar precipitation changes in ITA are primarily driven by the tropical easterly jet (TEJ)-dominated pattern, with a secondary contribution from the intertropical convergence zone (ITCZ)-mediated pattern. The Indo-Pacific warming-induced TEJ strengthening favors a monopolar drying trend from 1950 to 2022, while the northward-shifted ITCZ drives a west drying-east wetting dipolar pattern. Considering an observational TEJ constraint, an accelerated TEJ with an amplitude of -2 standard deviations could cause an almost threefold increase in extreme drying trends in the near term (2026-2045). Instead, ITA could face a higher likelihood of extreme wetting tendency due to a near-term TEJ weakening. Our findings underscore the importance of realistic TEJ simulations in enhancing confidence in future precipitation projections across hydroclimate-vulnerable Africa. (200 words)

Introduction

The agriculture-dependent socioeconomic livelihoods in Africa are highly susceptible to precipitation variations during the boreal spring crop-growing season^{1, 2} (March-May). Climatologically, intense spring precipitation predominantly occurs in the inter-tropical African domain³ (ITA: 12°S-12°N, as demarcated in Fig. 1 and Supplementary Fig. 1), encompassing the Great Horn of Africa. Remarkable shifts in ITA spring precipitation regimes over historical intervals have sparked pivotal research interests. Decadal shifts in the spring precipitation regime in ITA have engendered multifaceted socioeconomic impacts⁴, covering agriculture, economy, energy, ecosystems, the environment, and health. For instance, detrimental sequential droughts have swept ITA since the late 1990s (Fig. 1a and Supplementary Fig. 2), resulting in substantial losses of crop yields, livestock, and hydropower generation^{5, 6} due to a decline in potable water and aquifer recharge⁷ caused by rainfall deficits. These interlinked consequences push agriculture and pastoralist communities to the brink of acute food and freshwater shortages⁸, with the United Nations declaring a near-famine emergency. Accordingly, it is imperative to understand the historical aspects and mechanisms of the ITA precipitation regime shifts to enable timely adaptation actions.

The observed ITA spring precipitation exhibits considerable inter-decadal fluctuations, characterized by a prominent wetting tendency before the late 1990s and a persistent drying trend thereafter through the 2020s (Fig. 1a), albeit with occasional interruptions in individual years. These alternate wetting and drying episodes are prevalent across various observations^{2, 4, 9-13} and paleoclimate records¹⁴⁻¹⁶. Especially noteworthy is a spate of devastating droughts that have ravaged East Africa in recent decades, complicating the model-projected increase in precipitation response to greenhouse warming from the Coupled Model Inter-comparison Project (CMIP) of

previous generations^{11, 13, 17, 18} (CMIP3, CMIP5, and CMIP6). The glaring observation-model incongruence is referred to as the East Africa climate paradox¹¹, triggering a dramatic debate on the underlying mechanisms. One primary hypothesis links the decades-long droughts to the unusual Indo-western Pacific sea surface temperature (SST) warming^{1, 9, 19, 20} or tropical eastern Pacific cooling^{2, 10, 18, 21-24} via the intensification of the Indian Ocean Walker circulation^{20, 21}. The resulting enhanced subsidence suppresses precipitation in that area. Another hypothesis considers anthropogenic signals of East Africa drying, mainly due to the combined effects of greenhouse-gas-induced warming and aerosol-forced cooling, which increase evaporative demand^{14, 25}. Nevertheless, the key mechanism governing historical changes in precipitation regime has not been rigorously quantified due to model deficiencies in reproducing the timing and magnitude of ITA precipitation changes.

Climate models from CMIP3 to CMIP6 consistently project increasing precipitation^{13, 17, 18} in ITA over the past through the 21st century, casting doubt on near-term precipitation projections. To implement viable mitigation strategies across ITA, which is facing growing threats to food and water resource security, narrowing near-term projected precipitation uncertainty is indispensable, given a comprehensive understanding of the dynamics driving decadal shifts in the ITA precipitation regime. Here, we present observational evidence that two leading precipitation modes regulate decadal changes in observed ITA spring precipitation. The two modes are associated with the tropical easterly jet (TEJ) strengthening owing to Indian Ocean-western Pacific warming and a northward-shifted Inter-tropical Convergence Zone (ITCZ) modulated by a north-minus-south inter-hemispheric warming contrast, respectively, with the first mode being dominant. Our findings demonstrate that uncertainty in near-term projected ITA precipitation under high-emission scenarios greatly diminishes after correction using the observed TEJ.

Results

Two distinct precipitation regimes

We characterize observed spatiotemporal variations of ITA precipitation on inter-decadal timescales by applying an empirical orthogonal function (EOF) analysis to MAM-averaged precipitation anomalies in ITA (12°S - 12°N , 16°W - 52°E ; excluding coastal or oceanic grids) during 1950-2022 (Methods). The first leading mode ($\sim 32.2\%$ of the total variance) features a monopolar pattern of same-sign precipitation anomalies across ITA (Fig. 1b), except for a narrow strip along the coast of Equatorial Guinea. The corresponding principal component (PC1) delineates a gradual drop from 1950 to 2022, nearly in phase with the inter-decadal fluctuations of the observed TEJ strength (Fig. 1d). Because the first mode is strongly correlated with the TEJ, with a correlation coefficient of ~ 0.89 ($P < 0.01$), we refer to it as the TEJ-dominated precipitation regime. The second mode ($\sim 15.1\%$) resembles a northwest-southeast-oriented dipole-like pattern of opposite-sign precipitation anomalies (Fig. 1c). The corresponding time series are more synchronous with inter-decadal changes in the ITCZ location ($R = \sim 0.58$, $P < 0.01$) and the north-minus-south inter-hemispheric temperature contrast ($R = \sim 0.77$, $P < 0.01$), referred to as the ITCZ-mediated precipitation regime (Fig. 1e). Consistently, the TEJ-dominated monopolar and ITCZ-mediated dipole-like precipitation regimes are readily discernible from the Climatic Research Unit (CRU) high-resolution gridded precipitation dataset (Supplementary Fig. 3).

The two distinct precipitation patterns also manifest in other precipitation products from diverse data sources (Supplementary Fig. 4), albeit with spatial heterogeneity of precipitation variations. Furthermore, they are not highly sensitive to the size of the analyzed domain or shorter study periods (Methods). The broad agreement between two major modes across observations

confirms that the TEJ-dominated and ITCZ-mediated precipitation regimes adequately anchor inter-decadal variations in observed ITA spring precipitation. Based on the two distinct precipitation regimes, we reliably reconstruct the ITA spring precipitation anomalies for 1950–2022 (Fig. 1a), as corroborated by a high correlation with the original precipitation time series ($R = \sim 0.9$, $P < 0.01$). Notably, the original precipitation spatiotemporal variations better match the TEJ-dominated regime in terms of the decadal-timescale shifts (cf. Fig. 1a, d) and spatially homogeneous drying conditions inferred from the first-mode reconstruction alone (cf. Fig. 2a and Supplementary Fig. 2), indicating that inter-decadal changes in the ITA spring precipitation are principally controlled by the TEJ evolution (Fig. 1 and Supplementary Fig. 3), with an additional influence from a meridional excursion of the ITCZ.

Competing impacts of TEJ and ITCZ

We further unravel the dynamic processes for the dominance of TEJ over the large-scale precipitation decline pattern in ITA. We first quantify the observed ITA precipitation changes linearly congruent to the TEJ evolution by regressing the observed spring precipitation field onto the 9-year running-mean TEJ index and then multiplying the corresponding regression coefficients at each grid by the TEJ trends from 1950 to 2022 (termed TEJ-induced precipitation; see Methods). The accelerated TEJ reduces vertical moisture advection via anomalous subsidence (Fig. 2c, d), thus producing large-scale drying conditions across ITA (Fig. 2b and Supplementary Fig. 5).

To identify the robustness of the TEJ governing long-term precipitation changes in ITA, we decompose precipitation changes into dynamic (atmospheric circulation changes) and thermodynamic (atmospheric moisture content changes) components during 1950–2022 using the atmospheric column-integrated moisture budget^{26, 27} (Methods). The long-term decline in net ITA

precipitation is strongly linked to decreased vertical moisture advection²⁸ (Fig. 2e), particularly the dynamic component induced by increased subsidence. More specifically, weakened vertical moisture advection linked to enhanced subsidence across large swaths of ITA contributes to the monopole-like drying pattern (Fig. 2f, g). The converse holds for positive precipitation anomalies in Equatorial Guinea. The physical consistency between the TEJ linear congruence and atmospheric moisture budget analyses demonstrates the dynamic control of TEJ in the long-term precipitation reduction over ITA (Fig. 2 and Supplementary Fig. 5).

The observed TEJ intensification is closely tied to enhanced equatorial planetary waves²⁹ for the period 1950-2022 (Supplementary Fig. 6), characterized by tropical tropospheric upper-level reversed-sign temperature signatures with significant warming at 200 hPa and cooling at 100 hPa (Supplementary Fig. 6c, d). Earlier studies have documented the linkage between increased equatorial planetary waves and SST anomalies in the Indo-western Pacific warm pool²⁹ or the tropical eastern Pacific³⁰⁻³². To elucidate the origin of TEJ strengthening, we analyze three pacemaker experiments with CESM1 (Methods) wherein SST anomalies in the tropical Indian Ocean-western Pacific, tropical eastern Pacific, and North Atlantic are separately nudged toward observations. Anomalous spring warming across the tropical Indian Ocean-western Pacific and eastern Pacific creates an accelerated TEJ (-0.113 and -0.107 ms⁻¹/10yr in Supplementary Fig. 7), collectively explaining ~50% of the observed (-0.458 ms⁻¹/10yr) and thus suggesting increased equatorial planetary waves of similar tropospheric upper-level opposite-sign temperature structures to observations (cf. Supplementary Figs. 6-7). Conversely, North Atlantic warming weakens the TEJ.

Remarkably, tropical Indian Ocean-western Pacific warming stimulates anomalous easterlies occupying the tropical Indian Ocean-western Pacific and anomalous westerlies

traversing the tropical eastern Pacific-Atlantic Oceans. By comparison, tropical eastern Pacific warming generates easterly anomalies traversing the tropical Atlantic to the Indian Ocean (Supplementary Fig. 7). Such favorable circulation conditions intensify tropospheric upper-level easterlies²⁴, large-scale convergence, and subsidence across ITA (Supplementary Fig. 6g, h), consequently suppressing precipitation. These results of a causal chain highlight a major control of TEJ on long-term drying in ITA, which is quite distinct from the modulation of low-level easterlies³³⁻³⁵ or the strengthening of the Indian Ocean walker circulation^{20, 21} (Supplementary Fig. 8) on the inter-annual drying conditions in East Africa.

While an intensified TEJ caused by the Indo-Pacific warming directly governs a broad-scale long-term drying across ITA, a north-south swing of the ITCZ^{36, 37} associated with inter-hemispheric thermal contrast indirectly stimulates a dipole-like precipitation pattern of inter-decadal changes (Fig. 3a-b and Supplementary Fig. 9). Anomalous north-minus-south inter-hemispheric SST gradients facilitate a northward-displaced ITCZ (Fig. 3a and Supplementary Fig. 9a) and a reduced Northern Hadley cell (Supplementary Fig. 10), coupling to the strengthened Walker cells across tropical oceans. The global reorganization of meridional- and zonal-overturning atmospheric circulations mirrors an energy balance between the increased northward oceanic heat transport from the Southern Hemisphere and the north-to-south cross-equatorial atmospheric heat flux^{38, 39}. Correspondingly, cross-equatorial surface wind anomalies are well established. Accelerated easterlies over the tropical eastern Pacific transport moisture-rich air northward across the equator and join an anomalous cyclone within the subtropical North Pacific warm SST. The associated humid air deflects into the tropical Indian Ocean along the northwestern flank of the cyclone. Enhanced southeasterlies over the tropical Indian Ocean also advect moisture northwards and converge with the northwesterly flow from a weak cyclonic circulation linked to

the high surface temperature¹² over the Arabian Peninsula and Arabian Sea (Fig. 3b), eventually fueling more precipitation across East Africa and the northern Indian Ocean. By comparison, intensified westerlies across the equatorial Atlantic, alongside an anomalous cyclone linked to warming in the tropical North Atlantic and the Sahara, draw moisture southwards away from northwestern Africa and into South Africa, contributing to drying conditions in northwest Africa and wetting conditions over South Africa. As such, the contrasting inter-hemispheric moisture flows interact and jointly shape the dipolar pattern of northwest drying and southeast wetting.

The dipole-like precipitation pattern typically manifests in significant regression and correlation between spring precipitation anomalies and the ITCZ and north-minus-south inter-hemispheric SST gradient metrics (Fig. 3 and Supplementary Fig. 10). The mechanical robustness highlights the dynamic adjustment of the ITA dipole-like precipitation pattern in response to the inter-hemispheric temperature contrast through a meridional migration of the ITCZ. When the Northern Hemisphere is relatively warmer, the ITCZ-mediated precipitation anomalies exacerbate the TEJ-driven drying in northwest Africa but partly mitigate drying across East and South Africa (Fig. 3a). The reverse occurs for a comparatively warmer Southern Hemisphere. The spring inter-hemispheric thermal contrast during 1950-2022 probably results from spatially inhomogeneous anthropogenic aerosol emissions⁴⁰⁻⁴² (Supplementary Fig. 11), which indirectly mediates the inter-hemispheric ITCZ shifts through aerosol-cloud interactions⁴³.

An observational TEJ constraint on historical and near-term precipitation changes

Our results show that TEJ evolution associated with the Indo-Pacific warm pool warming modulates decadal changes in observed spring precipitation across ITA. Nonetheless, because the simulated TEJ strength and its decadal effect on ITA precipitation are comparatively weaker than

observations (Supplementary Fig. 12), two single-model and CMIP6 multi-model ensemble simulations over historical intervals and under high-emission scenarios reproduce a sustained wetting tendency, leaving near-term precipitation projections highly uncertain. Given the TEJ dominance over ITA spring precipitation, we can apply an observed TEJ constraint to correct historical precipitation changes and near-term projections. It is worth noting that our observational TEJ constraint framework preserves the coherence of the atmospheric energy and moisture budget in each member/model after adjustment. Within an energetic framework⁴⁴, we do not alter the column-integrated diabatic cooling and the dry static energy transport by the mean circulation, thus maintaining an equilibrium energy balance of the atmosphere and the surface. From a moisture budget perspective, we do not deteriorate the dynamic component linked to the mid-troposphere vertical velocity and the thermodynamic component related to the lower-troposphere moisture content (see Fig. 2).

We first quantify the influence of TEJ evolution on historical precipitation changes by replacing the simulated TEJ trend in each member/model with the observed TEJ trend for the entire period (1950-2022 for ERA5 and 1958-2022 for JRA55). When we substitute the TEJ-related precipitation changes in each member/model with those generated by the observed TEJ evolution (Methods), all the models congregate on a greater probability of aggravated ITA drying trends (Fig. 4a-c and Supplementary Fig. 13a-c). To further illustrate the impact of TEJ on the spatiotemporal changes in simulated precipitation, we select eight members/models that show the largest strengthening of the simulated TEJ decadal effect on ITA precipitation (Methods). After the observed TEJ adjustment, the simulated drying trends are broadly comparable to the observed TEJ-induced precipitation decline (Fig. 4d). The adjusted precipitation patterns in all modes more closely align with observations (Supplementary Fig. 14), particularly in East Africa.

In the near term (2026-2045), we might expect persistent droughts or a reversal to more precipitation under high-emission scenarios, as the TEJ evolution could completely negate or amplify the externally forced wetting response. To understand how the TEJ modulates evolving probabilities of near-term precipitation projections, we remove the simulated precipitation changes that are linearly congruent to the TEJ in each member/model (Methods). The standard deviations (SDs) of precipitation trends during 2026-2045 across all models substantially decrease by 19% to 39.7% (Fig. 4e), suggesting that uncertainty in near-term projected precipitation partially stems from the simulated TEJ evolution. Next, we estimate the SD of the observed TEJ in ERA5 during 1950-2022 (1958-2022 for JRA55) and assume that the TEJ will vary from -1SD to +1SD or between +1SD and -1SD. The TEJ evolution of 2SD for 2026-2045 ($\pm 1.1 \text{ ms}^{-1}/10\text{yr}$ for ERA5 and $\pm 0.73 \text{ ms}^{-1}/10\text{yr}$ for JRA55) contains the observed TEJ trend ($-0.4 \pm 0.08 \text{ ms}^{-1}/10\text{yr}$ for ERA5 and $-0.17 \pm 0.09 \text{ ms}^{-1}/10\text{yr}$ for JRA55), thus representing a plausible future trajectory. We adjust the original TEJ-related precipitation changes in each member/model with those driven by the presumed fixed TEJ evolution (Methods). If a TEJ shifts from -1SD toward +1SD during 2026-2045, the chance of ITA drying will decrease from 44.44% to 36.84% (Fig. 4f), with a much higher likelihood of extreme wetting trends (11.11% to 28.07% in Fig. 4f and 11.11% to 16.96% in Supplementary Fig. 13d) compared to drying trends (9.94% to 19.88% in Fig. 4f and 9.94% to 15.79% in Supplementary Fig. 13d). By contrast, provided an accelerated TEJ with an amplitude of -2SD persists, the drying probability will greatly increase to 62%, with a nearly threefold increase in the chance of extreme drying trends (9.94% to 28.65% in Fig. 4f). The constrained near-term precipitation projections suggest a more likely drying future in hydroclimate-fragile Africa.

Discussion

ITA has experienced an extensive precipitation deficit since the 1990s, contrary to a model-projected past-to-future wetter response to anthropogenic warming¹³ in CMIP6. Observed decadal shifts in the spring precipitation regime are primarily caused by the enhanced TEJ due to Indo-Pacific warm pool warming, with a secondary influence from the northward-shifted ITCZ linked to an anomalous north-minus-south inter-hemispheric warming contrast. Given the dominance of TEJ over ITA precipitation decadal changes, we propose an observational TEJ constraint framework to narrow model spread and uncertainty in historical and near-future precipitation changes. The evolving TEJ has exacerbated the decline in spring precipitation from 1950 to 2022 and is likely to further contribute to a drier future in the near term (2026-2045). These findings enhance confidence in minimizing risks associated with increased hydroclimate volatility⁴⁵ across Africa under greenhouse warming.

Our study raises an intriguing question: what modulates the observed TEJ strength? The spring TEJ intensity is highly correlated with the African easterly jet (AEJ; $R = \sim 0.81$, $P < 0.01$) and tropical Indo-western Pacific warm pool SST ($R = -0.74$, $P < 0.01$). As earlier studies have reported that the TEJ is less influenced by latent heat release linked to convection⁴⁶ and the AEJ is mainly regulated by the latitudinal temperature gradients between the Sahara and the Atlantic to the south⁴⁷, we may rule out the possibility of the TEJ-AEJ interactions. Additionally, the AEJ and TEJ evolutions produce distinct precipitation responses across the ITA. The accelerated AEJ transports horizontal moisture flux into the equatorial Atlantic and Congo basin from East Africa³³ and thus contributes to recent East African drying. However, the strengthened TEJ suppresses vertical moisture advection via anomalous subsidence (recall Fig. 2), leading to broad drying in ITA. Also, the TEJ strength is weakly correlated with the Northern Hemisphere-minus-Southern

Hemisphere inter-hemispheric internal contrast ($R = -0.35, P < 0.05$) and the meridional surface temperature contrast between North Africa and inter-tropical Africa ($R = -0.4, P < 0.01$). These observational arguments suggest that the TEJ intensification ultimately stems from remote forcing of tropical Indo-western Pacific warming.

While previous studies emphasize an anthropogenic origin of the Indo-western Pacific warming⁴⁸, climate models project a weakened TEJ under greenhouse warming (Supplementary Fig. 7a), in stark contrast to the Indo-Pacific warming-induced TEJ intensification observed in our pacemaker experiments. The seeming paradox suggests that the intensified TEJ emerges as a dynamic adjustment to Indo-Pacific warming rather than a direct response to greenhouse gases⁴⁶. Current climate models misrepresent the bottom-up tropospheric processes⁴⁹ across the Indo-Pacific warm pool, thereby underestimating the simulated TEJ strength. Moreover, the simulated TEJ decadal effect on ITA precipitation changes is also substantially underestimated due to the weak connection of TEJ to ITA spring precipitation in climate models (Supplementary Fig. 12). Regarding our knowledge gap in regional climate dynamics^{50, 51}, systematic model biases¹¹, sparse rainfall-gauge observations⁵², and intricate terrains⁴ across ITA, convection-permitting high-resolution models⁵³ may provide an impetus to advance seasonal precipitation forecast capacities.

Due to unrealistic atmospheric and oceanic states in process-based modeling, skillful rainfall forecasts in ITA remain a challenge. Differentiable modeling⁵⁴, which combines physical models with machine learning, offers significant opportunities to bridge knowledge gaps and enhance predictive capabilities. This transformative approach could help deliver proactive climate information to disaster-prone African societies in a more interpretable, highly efficient way. An improved understanding of more plausible future trajectories of hydroclimate will benefit agrarian and pastoral practices in rain-fed Africa, which now faces an urgent need to formulate effective

adaptation actions to enhance the climate resilience of agriculture, infrastructure, and economic development.

Methods

Observations and reanalyses

Nine monthly precipitation products are analyzed here, including the European Centre for Medium-Range Weather Forecasts fifth-generation atmospheric reanalysis (ERA5)⁵⁵ on a $0.25^\circ \times 0.25^\circ$ horizontal resolution for 1950-2022, the Global Precipitation Climatology Center version 7 (GPCC)⁵⁶ with a $0.5^\circ \times 0.5^\circ$ grid for 1891-2020, the Climatic Research Unit TS version 4.09 (CRU)⁵⁷ with a $0.5^\circ \times 0.5^\circ$ grid for 1901-2022, the University of Delaware Terrestrial precipitation version 5.01 (UDEL)⁵⁸ on a $0.5^\circ \times 0.5^\circ$ grid for 1901-2017, the NOAA 20th-century reanalysis version 3 (20CV3)⁵⁹ with a $1^\circ \times 1^\circ$ horizontal resolution for 1806-2015, the Global Precipitation Climatology Project version 3.2 (GPCP)⁶⁰ on a $2.5^\circ \times 2.5^\circ$ spatial resolution for 1979-2022, the Climate Prediction Center Merged Analysis of Precipitation (CMAP) dataset⁶¹ with a $2.5^\circ \times 2.5^\circ$ spatial resolution for 1979-2022, the 55-year modern Japanese Reanalysis (JRA55)⁶² on a $1.25^\circ \times 1.25^\circ$ spatial resolution for 1958-2022, and the Modern-Era Retrospective analysis for Research and Applications version 2 (MERRA2)⁶³ with a $0.5^\circ \times 0.5^\circ$ spatial resolution for 1980-2022. All datasets are linearly regridded to a common $1^\circ \times 1^\circ$ resolution for visual purposes. These precipitation datasets are employed to examine the boreal spring precipitation climatology of 1981-2010 over inter-tropical Africa (ITA: $12^\circ\text{S}-12^\circ\text{N}$, outlined in Fig. 1 and Supplementary Fig. 1), estimate long-term variations in the spring precipitation during 1950-2022 (Supplementary Fig. 2), and determine the spring precipitation dominant modes across ITA (Fig. 1 and Supplementary Figs. 3-4).

Note that climatologically, prominent seasonal precipitation³ mainly occurs across ITA. The ITA depicts bimodal rainfall variability during boreal spring and summer (July-September: JAS; Supplementary Fig. 1). Whilst current climate models simulate summer precipitation

variations in ITA over the historical interval^{13, 17, 18} relatively well, they struggle to capture decadal shifts in the ITA spring precipitation regime, especially the past decades-long severe droughts (Supplementary Fig. 2). Additionally, historical precipitation projections of drought for southern Africa largely agree with the instrumental record¹⁴. Thus, our study mainly focuses on decadal shifts in the spring precipitation regime across ITA.

Atmospheric circulation, tropospheric temperature, and specific humidity fields from ERA5 and JRA55 are utilized to unravel the dynamical processes underlying two spring precipitation regimes (Figs. 1-2 and Supplementary Figs. 5-6). The Extended Reconstructed Sea Surface Temperature⁶⁴ version 3 (ERSST v3) on a $2^\circ \times 2^\circ$ grid, the Hadley Center Sea Ice and SST (HadISST) dataset⁶⁵ with a $1^\circ \times 1^\circ$ grid, the merged land-surface air temperature and SST dataset version 5 from the Met Office Hadley Centre (HadCRUT5)⁶⁶, and the National Oceanic and Atmospheric Administration (GlobalTemp)⁶⁷ during 1950-2022 are used to diagnose the north-south inter-hemispheric warming contrast that affects the ITCZ-mediated precipitation mode (Figs. 1 and 3 and Supplementary Figs. 9-11). Unless otherwise specified, our main results of the spring precipitation and atmospheric circulation diagnosis are based on ERA5 due mostly to its sufficient time length.

EOF analyses

We conduct an Empirical Orthogonal Function (EOF) analysis of observed spring precipitation anomalies over ITA (12°S - 12°N , 16°W - 52°E ; excluding coastal or oceanic grids) in each dataset to extract the dominant variability in precipitation. Based on the North et al. criterion⁶⁸, the first two EOFs in ERA5, representing the TEJ-dominated and ITCZ-mediated precipitation patterns (Fig. 1 and Supplementary Fig. 3), are distinctly separated from the remaining eigenvectors and

totally explain \sim 47.3% of the inter-decadal variance. Although the ensuing five EOFs (from EOF3 to EOF7) also meet the criterion, their explaining variance substantially decreases from 7.9% to 2.3%. Thus, we primarily focus on the first two precipitation regimes, which strikingly capture the long-term and inter-decadal precipitation variability in ITA and are quite evident across different datasets and during different analyzed periods (Supplementary Figs. 3-4). Similar results are obtained from larger (15°S - 15°N , 20°W - 52°E or 20°S - 20°N , 20°W - 52°E or 40°S - 20°N , 20°W - 52°E) or smaller (10°S - 10°N , 16°W - 52°E) domains with and without coastal or oceanic grids selected to perform an EOF analysis.

After reconstructions from the two leading precipitation regimes, the time series of spring precipitation anomalies averaged over ITA are highly correlated with the original results (Fig. 1a), with a correlation coefficient of \sim 0.99 ($P < 0.01$). Moreover, when the first precipitation mode is incorporated solely into reconstructions, the reconstructed ITA spring precipitation shows a long-term drying trend (Fig. 2a), consistent with the observed broad-scale drying (Supplementary Fig. 2).

CMIP6 and single-model large ensemble simulations

Using 31 models participating in the Coupled Model Intercomparison Project phase six (CMIP6), we examine the historical simulations for 1950-2014 and future projections under the Shared Socioeconomic Pathway 2-Representative Concentration Pathway 4.5 (SSP2-4.5) for 2015-2022 and SSP5-8.5 for 2015-2100. Historical simulations are forced by both the natural and anthropogenic radiative forcings. Only the first realization for each model is analyzed. These multi-model simulations provide a quantitative evaluation of not only the climatology of and long-term changes in spring precipitation over ITA during historical periods (Supplementary Figs. 1-2)

but also the near-term projections (Fig. 4, Supplementary Figs. 11-14, and Supplementary Fig. 16). We also use two sets of large ensemble initial-condition simulations with CESM1 and MPI-ESM-LR from the US CLIVAR Working Group to provide the spring precipitation climatology and future projections (Fig. 4 and Supplementary Figs. 11-14). These single-model simulations are forced by historical radiative forcing for 1950-2005 and under the RCP8.5 for 2006-2100 following the CMIP5 (Ref. ⁶⁹). To assess the respective role of different forcings in driving the tropical easterly jet (TEJ) during 1950-2022, we investigate 10 CMIP6 models with single-forcing simulations from the Detection and Attribution Model Intercomparison Project⁷⁰, including all external forcing (All), aerosol-only forcing (Aer), and greenhouse-gas-only forcing (GHG) simulations. A detailed description of the models is listed in Supplementary Tables 1-2.

Time-evolving pacemaker experiments

To unravel the potential drivers of the observed TEJ strengthening from 1950 to 2022, we examine three sets of 10-member ensemble pacemaker experiments with the fully coupled climate model CESM1 using the earlier methodology^{71, 72}. In these simulations (Supplementary Table 3 and Supplementary Fig. 15), SST anomalies over the tropical Indian Ocean-Western Pacific (IOWP: 15°S-15°N, African coast to 174°E with 5° buffer zones), tropical eastern Pacific (TEP: 15°S-15°N, 180° to the American coast with 5° buffer zones), and North Atlantic Ocean (NAT: 5°-55°N, the American coast to Africa/Europe with 5° tapering buffer zones) are separately restored to follow the observed history (ERSST V3). Beyond restoring domains, the ocean-atmosphere coupling systems are free to evolve. Each experiment is also forced by historical radiative forcing (1920-2005) and the RCP8.5 emission scenario (2006-2013), and initialized with micro-perturbations in the atmospheric conditions. The pacemaker experimental setup has reasonably reproduced the

three tropical ocean interactions⁷³ and tropical-southern ocean trans-hemispheric teleconnections⁷⁴, enabling us to systematically evaluate the extent to which SST variability in individual ocean basins forces the observed TEJ changes (Supplementary Fig. 7).

TEJ, ITCZ, and inter-hemispheric SST gradient metrics

The TEJ core resides near the equator in the boreal springtime for the climatology of 1981-2010 (Supplementary Fig. 5). Its location on the axis is largely unchanged for 1950-2022. The TEJ strength index⁷⁵ is expressed as the area-averaged 150-hPa zonal winds over the domain (8°S-8°N, 8°E-180°E). Negative values suggest a strengthened TEJ and vice versa. Note that climatological distributions of zonal winds, the strength, and the core axis location of TEJ are similar at 150 and 200 hPa levels. Thus, our main results are consistent for the TEJ defined based on 150-hPa and 200-hPa zonal winds.

To better understand factors regulating the TEJ intensity, we also discuss the relationship between the TEJ strength and the tropical Indo-western Pacific warm pool, the African easterly jet (AEJ), the inter-hemispheric thermal contrast, and the African meridional surface temperature contrast. The tropical Indo-western Pacific warm pool index is defined as the area-averaged SST (20°S-20°N, 30°E-180°E). The AEJ is defined as the area-averaged 700-hPa zonal winds (5°S-15°N, 10°W-20°E)⁴⁷. The inter-hemispheric thermal contrast is defined as the difference in area-averaged surface temperature between (20°N-50°N, 0°-360°) and (20°S-50°S, 0°-360°). The African meridional surface temperature contrast is defined as the area-averaged surface temperature difference between northern Africa (15°N-30°N, 10°W-60°E) and inter-tropical Africa (12°S-12°N, 10°W-20°E).

We adopt the latitudinal centroid of tropical spring precipitation to measure the zonal-mean

location of the ITCZ⁷⁶. Specifically, the ITCZ latitude (ϕ_{cent}) is calculated from the weighting function, with an integer power (N) of the area-weighted spring precipitation (P) integrated between the latitudinal bounds ($\phi_1=20^{\circ}\text{S}$ and $\phi_2=20^{\circ}\text{N}$) as follows:

$$\phi_{cent} = \frac{\int_{\phi_1}^{\phi_2} \phi [\cos(\phi)P]^N d\phi}{\int_{\phi_1}^{\phi_2} [\cos(\phi)P]^N d\phi} \quad (1)$$

Since the tropical precipitation centroid better captures the ITCZ variations across the seasonal to longer timescales⁷⁷⁻⁷⁹, we use the tropical spring precipitation centroid ($N=1$) to determine its linkage to the ITA spring precipitation dipole-like pattern on inter-decadal timescales (Fig. 1c, e), with a correlation coefficient of ~ 0.58 ($P < 0.01$). When $N = 2, 3$, or 4 , the correlation coefficients are approximately $0.52, 0.46$, and 0.41 , respectively. The high correlation coefficients suggest that our main results are insensitive to the choice of N . The monthly precipitation is linearly interpolated to a $0.1^{\circ} \times 0.1^{\circ}$ spatial resolution to minimize potential grid dependence before calculating the ITCZ centroid index. Our main results hold when integrating the domains equatorward of 15° and 30° in each hemisphere.

Previous studies have revealed that the seasonal migration of the ITCZ location is strongly linked to atmospheric heat transport at the equator (anticorrelation) and the inter-hemispheric tropical SST warming contrast (positive correlation) in both observations and coupled models⁷⁸. For a visual comparison with the ITCZ-mediated precipitation regime (Fig. 1e), we calculate the north-minus-south inter-hemispheric SST gradient (NH-SH SST) as the difference between the area-weighted SST of $30^{\circ}\text{N}-60^{\circ}\text{N}$ minus $-30^{\circ}\text{S}-0^{\circ}$. Notably, the tropical SST mean ($20^{\circ}\text{S}-20^{\circ}\text{N}$) has been removed to accentuate the inter-hemispheric thermal contrast.

TEJ-induced precipitation changes

To quantify the direct impact of TEJ on long-term changes in the observed ITA spring precipitation,

we first regress the observed spring precipitation field onto the 9-year moving-mean spring TEJ index for 1950-2022. We then multiply regression coefficients at each grid by the TEJ time series to provide a projection of the spring precipitation field onto the TEJ index. Finally, we estimate linear trends for the corresponding projection, representing the spring precipitation trends statistically associated with the TEJ changes (Fig. 2b). We further apply the same procedure to the vertical moisture advection and 500-hPa vertical velocity (Fig. 2c-d and Supplementary Fig. 5) to unravel physical processes for the TEJ driving long-term drying across ITA.

Atmospheric moisture budget analysis

To disentangle the key physical processes governing ITA precipitation long-term changes related to the TEJ-dominated precipitation regime (Fig. 2), we partition precipitation changes into thermodynamic (atmospheric moisture changes) and dynamic (atmospheric circulation changes) components based on the atmospheric column-integrated moisture budget^{26, 27} as follows:

$$P' - E' = -\langle \vec{V}_h \cdot \nabla_h q \rangle' - \langle \omega \partial_p q \rangle' + \delta' \quad (2)$$

where P and E are precipitation and evaporation, respectively; \vec{V}_h , ω , and q represent the horizontal and vertical pressure-level velocity and specific humidity, respectively; δ is a residual term largely because of sub-seasonal transient eddies, surface processes caused by the complex topography, and even moisture storage. The prime denotes the monthly anomaly referenced to the climatological mean of 1981-2010, and the angular brackets indicate vertical-column integration for the entire troposphere. Here, we aim to quantify the relative importance of different moisture advection terms to the effective atmospheric moisture ($P' - E'$).

The horizontal and vertical moisture advection terms are further split into:

$$-\langle \vec{V}_h \cdot \nabla_h q \rangle' = -\langle \overline{\vec{V}_h} \cdot \nabla_h q' \rangle - \langle \vec{V}_h' \cdot \nabla_h \bar{q} \rangle - \langle \vec{V}_h' \cdot \nabla_h q' \rangle \quad (3)$$

$$-\langle \omega \partial_p q \rangle' = -\langle \bar{\omega} \nabla_h q' \rangle - \langle \omega' \nabla_h \bar{q} \rangle - \langle \omega' \nabla_h q' \rangle \quad (4)$$

The terms on the right-hand side of the equations comprise thermodynamic components directly affected by temperature-generated changes in atmospheric water vapor following the Clausius-Clapeyron relationship, dynamic components tied to changes in atmospheric circulation, and nonlinear effects.

An observational TEJ constraint framework for precipitation changes

By replacing the simulated TEJ-related precipitation trends in each member/model with those driven by the observed TEJ, we establish a process-based constraint framework for narrowing the spread in simulated historical precipitation changes and reducing uncertainty in near-term precipitation projections (Fig. 4), similar to an adjustment method⁸⁰ of adopting the observed Inter-decadal Pacific Oscillation to constrain the simulated Indian summer monsoon precipitation. This process-based constraint framework is expressed as follows:

$$\partial_t P_{constrained}(j) = \partial_t P_{original}(j) - R_{P,TEJ}(j) \cdot (\partial_t TEJ(j) - \partial_t TEJ_{obs}), j = 1, 2, \dots, n \quad (5)$$

Where $\partial_t P_{constrained}(j)$ and $\partial_t P_{original}(j)$ are the constrained and original spring precipitation trends during the study period in member/model j , respectively; $R_{P,TEJ}(j)$ is estimated as the area-averaged regression coefficients of the ITA spring precipitation field against the 9-year running-mean spring TEJ index, reflecting the sensitivity of spring precipitation to the TEJ evolution (termed the TEJ decadal effect) in member/model j ; $R_{P,TEJ}(j) \cdot \partial_t TEJ(j)$ is the original TEJ-induced precipitation trend in member/model j and $R_{P,TEJ}(j) \cdot \partial_t TEJ_{obs}$ indicates the precipitation trend related to the observed TEJ evolution.

To illustrate the potential impact of TEJ on near-term (2026-2045) spring precipitation projections (Fig. 4e), we compute the TEJ index in each member/model and then remove the spring

precipitation variations linearly congruent to the TEJ as follows:

$$\partial_t P_{non-TEJ}(j) = \partial_t P_{original}(j) - R_{P,TEJ}(j) \cdot \partial_t TEJ(j), j = 1, 2, \dots, n \quad (6)$$

After removing the simulated TEJ effect on precipitation across models, the standard deviation of simulated precipitation trends in the near term (2026-2045) decreases from 19% to 39.7% (Fig. 4e), supporting our notion that a plausible TEJ evolution can effectively reduce near-term projected precipitation uncertainty.

Moreover, we estimate the probability of ITA drying during 2026-2045 (Fig. 4f). The chance of decreasing precipitation trends in ITA is computed by dividing the number of members showing negative precipitation trends by the total members (i.e., 31 CMIP6 models, 40 CESM1 runs, and 100 MPI-ESM-LR runs). We calculate the probability of near-term drying for both the original and the constrained precipitation trends under a given TEJ evolution. We also compute the probability of precipitation trends below the 10th percentile of the original trends (denoted extreme drying, ED) and above the 90th percentile (denoted extreme wetting, EW). The chance of ED (EW) is estimated by dividing the number of members showing precipitation trends less than (greater than) or equal to the 10th (90th) percentile of the original trends by the total members. The probabilities of ED and EW are also calculated for constrained precipitation trends with a certain TEJ evolution.

Statistical analysis methods

We employ an ordinary least-squares linear fit to estimate linear trends (Figs. 2 and 4) with a 95% significance based on a two-sided Student's *t*-test. A 9-year running mean is used to extract inter-decadal signals from observations and models before calculating regression and correlation coefficients. The statistical significance of regression and correlation coefficients is also measured

using a two-sided Student's *t*-test.

Data availability

Observations and model outputs used in this study are publicly available from the following websites: ERA5 (<https://cds.climate.copernicus.eu/datasets/reanalysis-era5-single-levels-monthly-means?tab=download>); GPCC (<https://psl.noaa.gov/data/gridded/data.gpcc.html>); CRU (<https://crudata.uea.ac.uk/cru/data/hrg/>); UDEL (https://psl.noaa.gov/data/gridded/data.UDel_AirT_Precip.html); 20CV3 (https://psl.noaa.gov/data/gridded/data.20thC_ReanV3.html); GPCP (<https://psl.noaa.gov/data/gridded/data.gpcp.html>); CMAP (<https://psl.noaa.gov/data/gridded/data.cmap.html>); JRA55 (<https://rda.ucar.edu/datasets/ds628-1/>); MERRA2 (<https://gmao.gsfc.nasa.gov/reanalysis/MERRA-2/>); ERSST v3b (<https://www.ncei.noaa.gov/products/extended-reconstructed-sst>); HadISST (<https://www.metoffice.gov.uk/hadobs/hadisst/>); HadCRUT5 (<https://www.metoffice.gov.uk/hadobs/hadcrut5/>); NOAA GlobalTemp (<https://psl.noaa.gov/data/gridded/data.noaaglobaltemp.html>); CESM1 large ensemble outputs are available at <https://gdex.ucar.edu/gsearch/dataset-search/?q=CESM1+large+ensemble>. All the CMIP6 model outputs are available at <https://esgf-metagrid.cloud.dkrz.de/search>. The CESM1 pacemaker experiments used in this study are available upon request.

Code Availability

The codes required to generate all the figures are available upon request. The codes are created using the NCAR Command Language (NCL: <https://www.ncl.ucar.edu/>).

Acknowledgments

This work is supported by the National Key Program for Developing Basic Sciences (2020YFA0608902) and the National Key R&D Program of China (2022YFC3104805). We thank Dr. Shang-Ping Xie, Dr. Wenju Cai, and Dr. Qinghua Ding for their helpful comments and discussion on an early version of this study. We acknowledge the World Climate Research Programme working group on coupled modeling, which led the design of CMIP6 experiments and coordinated the work. We are also grateful to the individual climate modeling groups for their efforts in model simulations. We thank the Community Earth System Model (CESM) large ensemble community project and the Climate Variability and Change working group for making model output available.

Author contributions

S.L.Y. and R.W. conceived the study and wrote the draft. S.L.Y. conducted all the data analyses and produced the final figures. P.L., P.S.C., and H.T. provided comments and revised the manuscript. P.W. helped edit the manuscript. All authors contributed to the interpretation of the results.

Competing interests

The authors declare no competing interests.

References

1. Funk C, Dettinger MD, Michaelsen JC, Verdin JP, Brown ME, Barlow M, *et al.* Warming of the Indian Ocean threatens eastern and southern African food security but could be mitigated by agricultural development. *Proceedings of the national academy of sciences* 2008, **105**(32): 11081-11086.
2. Lyon B, DeWitt DG. A recent and abrupt decline in the East African long rains. *Geophysical Research Letters* 2012, **39**(2).
3. Preethi B, Sabin T, Adedoyin J, Ashok K. Impacts of the ENSO Modoki and other tropical Indo-Pacific climate-drivers on African rainfall. *Scientific reports* 2015, **5**(1): 16653.
4. Palmer PI, Wainwright CM, Dong B, Maidment RI, Wheeler KG, Gedney N, *et al.* Drivers and impacts of Eastern African rainfall variability. *Nature Reviews Earth & Environment* 2023, **4**(4): 254-270.
5. Adloff M, Singer MB, MacLeod DA, Michaelides K, Mehrnagar N, Hansford E, *et al.* Sustained water storage in Horn of Africa drylands dominated by seasonal rainfall extremes. *Geophysical Research Letters* 2022, **49**(21): e2022GL099299.
6. Conway D, Dalin C, Landman WA, Osborn TJ. Hydropower plans in eastern and southern Africa increase risk of concurrent climate-related electricity supply disruption. *Nature Energy* 2017, **2**(12): 946-953.
7. Taylor RG, Todd MC, Kongola L, Maurice L, Nahozya E, Sanga H, *et al.* Evidence of the dependence of groundwater resources on extreme rainfall in East Africa. *Nature Climate Change* 2013, **3**(4): 374-378.
8. Anderson W, Taylor C, McDermid S, Ilboudo-Nébié E, Seager R, Schlenker W, *et al.* Violent conflict exacerbated drought-related food insecurity between 2009 and 2019 in sub-Saharan Africa. *Nature Food* 2021, **2**(8): 603-615.
9. Liebmann B, Hoerling MP, Funk C, Bladé I, Dole RM, Allured D, *et al.* Understanding recent eastern Horn of Africa rainfall variability and change. *Journal of Climate* 2014, **27**(23): 8630-8645.
10. Lyon B. Seasonal drought in the Greater Horn of Africa and its recent increase during the March–May long rains. *Journal of Climate* 2014, **27**(21): 7953-7975.
11. Rowell DP, Booth BB, Nicholson SE, Good P. Reconciling past and future rainfall trends over East Africa. *Journal of Climate* 2015, **28**(24): 9768-9788.
12. Wainwright CM, Marsham JH, Keane RJ, Rowell DP, Finney DL, Black E, *et al.* ‘Eastern African Paradox’ rainfall decline due to shorter not less intense Long Rains. *npj Climate and Atmospheric Science* 2019, **2**(1): 34.

13. Schwarzwald K, Seager R. Revisiting the “East African Paradox”: CMIP6 models also struggle to reproduce strong observed Long Rain drying trends. *Journal of Climate* 2024, **37**(24): 6641-6658.
14. Baxter A, Verschuren D, Peterse F, Miralles D, Martin-Jones C, Maitiuerdi A, *et al.* Reversed Holocene temperature–moisture relationship in the Horn of Africa. *Nature* 2023, **620**(7973): 336-343.
15. Tierney JE, Smerdon JE, Anchukaitis KJ, Seager R. Multidecadal variability in East African hydroclimate controlled by the Indian Ocean. *Nature* 2013, **493**(7432): 389-392.
16. Tierney JE, Ummenhofer CC, Demenocal PB. Past and future rainfall in the Horn of Africa. *Science advances* 2015, **1**(9): e1500682.
17. Anyah RO, Qiu W. Characteristic 20th and 21st century precipitation and temperature patterns and changes over the Greater Horn of Africa. *International Journal of Climatology* 2012, **32**(3): 347-363.
18. Yang W, Seager R, Cane MA, Lyon B. The East African long rains in observations and models. *Journal of Climate* 2014, **27**(19): 7185-7202.
19. Hoell A, Funk C. Indo-Pacific sea surface temperature influences on failed consecutive rainy seasons over eastern Africa. *Climate dynamics* 2014, **43**: 1645-1660.
20. Williams AP, Funk C. A westward extension of the warm pool leads to a westward extension of the Walker circulation, drying eastern Africa. *Climate Dynamics* 2011, **37**: 2417-2435.
21. Funk C, Fink AH, Harrison L, Segele Z, Endris HS, Galu G, *et al.* Frequent but predictable droughts in East Africa driven by a Walker circulation intensification. *Earth's Future* 2023, **11**(11): e2022EF003454.
22. Funk C, Harrison L, Shukla S, Pomposi C, Galu G, Korecha D, *et al.* Examining the role of unusually warm Indo-Pacific sea-surface temperatures in recent African droughts. *Quarterly Journal of the Royal Meteorological Society* 2018, **144**: 360-383.
23. Hoell A, Hoerling M, Eischeid J, Quan X-W, Liebmann B. Reconciling theories for human and natural attribution of recent East Africa drying. *Journal of Climate* 2017, **30**(6): 1939-1957.
24. Liebmann B, Bladé I, Funk C, Allured D, Quan X-W, Hoerling M, *et al.* Climatology and interannual variability of boreal spring wet season precipitation in the eastern Horn of Africa and implications for its recent decline. *Journal of Climate* 2017, **30**(10): 3867-3886.
25. Allan RP, Barlow M, Byrne MP, Cherchi A, Douville H, Fowler HJ, *et al.* Advances in

understanding large-scale responses of the water cycle to climate change. *Annals of the New York Academy of Sciences* 2020, **1472**(1): 49-75.

26. Chou C, Lan C-W. Changes in the annual range of precipitation under global warming. *Journal of Climate* 2012, **25**(1): 222-235.
27. Seager R, Naik N, Vecchi GA. Thermodynamic and dynamic mechanisms for large-scale changes in the hydrological cycle in response to global warming. *Journal of climate* 2010, **23**(17): 4651-4668.
28. Kenfack K, Tamoffo AT, Tchotchou LAD, Marra F, Kaissassou S, Nana HN, *et al.* Processes behind the decrease in Congo Basin precipitation during the rainy seasons inferred from ERA-5 reanalysis. *International Journal of Climatology* 2024, **44**(5): 1778-1799.
29. Dima IM, Wallace JM. Structure of the annual-mean equatorial planetary waves in the ERA-40 reanalyses. *Journal of the atmospheric sciences* 2007, **64**(8): 2862-2880.
30. Rasmusson EM, Carpenter TH. Variations in tropical sea surface temperature and surface wind fields associated with the Southern Oscillation/El Niño. *Monthly Weather Review* 1982, **110**(5): 354-384.
31. Kraucunas I, Hartmann DL. Equatorial superrotation and the factors controlling the zonal-mean zonal winds in the tropical upper troposphere. *Journal of the atmospheric sciences* 2005, **62**(2): 371-389.
32. Grise KM, Thompson DW. Equatorial planetary waves and their signature in atmospheric variability. *Journal of the atmospheric sciences* 2012, **69**(3): 857-874.
33. Walker DP, Marsham JH, Birch CE, Scaife AA, Finney DL. Common mechanism for interannual and decadal variability in the East African long rains. *Geophysical Research Letters* 2020, **47**(22): e2020GL089182.
34. Finney DL, Marsham JH, Walker DP, Birch CE, Woodhams BJ, Jackson LS, *et al.* The effect of westerlies on East African rainfall and the associated role of tropical cyclones and the Madden-Julian Oscillation. *Quarterly Journal of the Royal Meteorological Society* 2020, **146**(727): 647-664.
35. Yang W, Seager R, Cane MA, Lyon B. The annual cycle of East African precipitation. *Journal of Climate* 2015, **28**(6): 2385-2404.
36. Kebacho LL, Chen H. The dominant modes of the long rains interannual variability over Tanzania and their oceanic drivers. *International Journal of Climatology* 2022, **42**(10): 5273-5292.
37. Kebacho LL, Mbigi D, Makula EK, Mangara RJ, Mteweze ZF, Kessy WP, *et al.* Decadal

shifts of the long rains in Tanzania and associated atmospheric circulation anomalies around 1999. *Theoretical and Applied Climatology* 2025, **156**(3): 1-19.

38. Schneider T, Bischoff T, Haug GH. Migrations and dynamics of the intertropical convergence zone. *Nature* 2014, **513**(7516): 45-53.
39. Orihuela-Pinto B, England MH, Taschetto AS. Interbasin and interhemispheric impacts of a collapsed Atlantic Overturning Circulation. *Nature Climate Change* 2022, **12**(6): 558-565.
40. Deser C, Phillips AS, Simpson IR, Rosenbloom N, Coleman D, Lehner F, *et al.* Isolating the evolving contributions of anthropogenic aerosols and greenhouse gases: A new CESM1 large ensemble community resource. *Journal of climate* 2020, **33**(18): 7835-7858.
41. Kang SM, Xie S-P, Deser C, Xiang B. Zonal mean and shift modes of historical climate response to evolving aerosol distribution. *Science Bulletin* 2021, **66**(23): 2405-2411.
42. Chiang JC, Friedman AR. Extratropical cooling, interhemispheric thermal gradients, and tropical climate change. *Annual Review of Earth and Planetary Sciences* 2012, **40**(1): 383-412.
43. Chung E-S, Soden BJ. Hemispheric climate shifts driven by anthropogenic aerosol–cloud interactions. *Nature Geoscience* 2017, **10**(8): 566-571.
44. Muller CJ, O’Gorman P. An energetic perspective on the regional response of precipitation to climate change. *Nature Climate Change* 2011, **1**(5): 266-271.
45. Swain DL, Prein AF, Abatzoglou JT, Albano CM, Brunner M, Diffenbaugh NS, *et al.* Hydroclimate volatility on a warming Earth. *Nature Reviews Earth & Environment* 2025, **6**(1): 35-50.
46. Nicholson SE, Klotter D. The Tropical Easterly Jet over Africa, its representation in six reanalysis products, and its association with Sahel rainfall. *International Journal of Climatology* 2021, **41**(1): 328-347.
47. Nicholson SE, Grist JP. The seasonal evolution of the atmospheric circulation over West Africa and equatorial Africa. *Journal of climate* 2003, **16**(7): 1013-1030.
48. Weller E, Min S-K, Cai W, Zwiers FW, Kim Y-H, Lee D. Human-caused Indo-Pacific warm pool expansion. *Science advances* 2016, **2**(7): e1501719.
49. Grise KM, Thompson DW. On the signatures of equatorial and extratropical wave forcing in tropical tropopause layer temperatures. *Journal of the Atmospheric Sciences* 2013, **70**(4): 1084-1102.
50. Kent C, Chadwick R, Rowell DP. Understanding uncertainties in future projections of

seasonal tropical precipitation. *Journal of Climate* 2015, **28**(11): 4390-4413.

51. Jiang J, Zhou T, Qian Y, Li C, Song F, Li H, *et al.* Precipitation regime changes in High Mountain Asia driven by cleaner air. *Nature* 2023, **623**(7987): 544-549.
52. Shiogama H, Watanabe M, Kim H, Hirota N. Emergent constraints on future precipitation changes. *Nature* 2022, **602**(7898): 612-616.
53. Prein AF, Langhans W, Fosser G, Ferrone A, Ban N, Goergen K, *et al.* A review on regional convection-permitting climate modeling: Demonstrations, prospects, and challenges. *Reviews of geophysics* 2015, **53**(2): 323-361.
54. Shen C, Appling AP, Gentine P, Bandai T, Gupta H, Tartakovsky A, *et al.* Differentiable modelling to unify machine learning and physical models for geosciences. *Nature Reviews Earth & Environment* 2023, **4**(8): 552-567.
55. Hersbach H, Bell B, Berrisford P, Hirahara S, Horányi A, Muñoz-Sabater J, *et al.* The ERA5 global reanalysis. *Quarterly Journal of the Royal Meteorological Society* 2020, **146**(730): 1999-2049.
56. Schneider U, Becker A, Finger P, Meyer-Christoffer A, Ziese M, Rudolf B. GPCC's new land surface precipitation climatology based on quality-controlled in situ data and its role in quantifying the global water cycle. *Theoretical and applied climatology* 2014, **115**: 15-40.
57. Harris I, Jones P, Osborn T, Lister D. Updated high-resolution grids of monthly climatic observations-the CRU TS3. 10 Dataset. *International journal of climatology* 2014, **34**: 623-642.
58. Parsons LA. Implications of CMIP6 projected drying trends for 21st century Amazonian drought risk. *Earth's Future* 2020, **8**(10): e2020EF001608.
59. Slivinski LC, Compo GP, Whitaker JS, Sardeshmukh PD, Giese BS, McColl C, *et al.* Towards a more reliable historical reanalysis: Improvements for version 3 of the Twentieth Century Reanalysis system. *Quarterly Journal of the Royal Meteorological Society* 2019, **145**(724): 2876-2908.
60. Adler RF, Sapiano MR, Huffman GJ, Wang J-J, Gu G, Bolvin D, *et al.* The Global Precipitation Climatology Project (GPCP) monthly analysis (new version 2.3) and a review of 2017 global precipitation. *Atmosphere* 2018, **9**(4): 138.
61. Xie P, Arkin PA. Global precipitation: A 17-year monthly analysis based on gauge observations, satellite estimates, and numerical model outputs. *Bulletin of the american meteorological society* 1997, **78**(11): 2539-2558.
62. Harada Y, Kamahori H, Kobayashi C, Endo H, Kobayashi S, Ota Y, *et al.* The JRA-55

Reanalysis: Representation of atmospheric circulation and climate variability. *Journal of the Meteorological Society of Japan Ser II* 2016, **94**(3): 269-302.

63. Gelaro R, McCarty W, Suárez MJ, Todling R, Molod A, Takacs L, *et al.* The modern-era retrospective analysis for research and applications, version 2 (MERRA-2). *Journal of climate* 2017, **30**(14): 5419-5454.

64. Huang B, Thorne PW, Banzon VF, Boyer T, Chepurin G, Lawrimore JH, *et al.* Extended reconstructed sea surface temperature, version 5 (ERSSTv5): upgrades, validations, and intercomparisons. *Journal of Climate* 2017, **30**(20): 8179-8205.

65. Titchner HA, Rayner NA. The Met Office Hadley Centre sea ice and sea surface temperature data set, version 2: 1. Sea ice concentrations. *Journal of Geophysical Research: Atmospheres* 2014, **119**(6): 2864-2889.

66. Morice CP, Kennedy JJ, Rayner NA, Winn J, Hogan E, Killick R, *et al.* An updated assessment of near-surface temperature change from 1850: The HadCRUT5 data set. *Journal of Geophysical Research: Atmospheres* 2021, **126**(3): e2019JD032361.

67. Vose RS, Arndt D, Banzon VF, Easterling DR, Gleason B, Huang B, *et al.* NOAA's merged land-ocean surface temperature analysis. *Bulletin of the American Meteorological Society* 2012, **93**(11): 1677-1685.

68. North GR, Bell TL, Cahalan RF, Moeng FJ. Sampling errors in the estimation of empirical orthogonal functions. *Monthly weather review* 1982, **110**(7): 699-706.

69. Taylor KE, Stouffer RJ, Meehl GA. An overview of CMIP5 and the experiment design. *Bulletin of the American meteorological Society* 2012, **93**(4): 485-498.

70. Gillett NP, Shiogama H, Funke B, Hegerl G, Knutti R, Matthes K, *et al.* The detection and attribution model intercomparison project (DAMIP v1. 0) contribution to CMIP6. *Geoscientific Model Development* 2016, **9**(10): 3685-3697.

71. Deser C, Guo R, Lehner F. The relative contributions of tropical Pacific sea surface temperatures and atmospheric internal variability to the recent global warming hiatus. *Geophysical Research Letters* 2017, **44**(15): 7945-7954.

72. Meehl GA, Hu A, Castruccio F, England MH, Bates SC, Danabasoglu G, *et al.* Atlantic and Pacific tropics connected by mutually interactive decadal-timescale processes. *Nature Geoscience* 2021, **14**(1): 36-42.

73. Yao S-L, Luo J-J, Chu P-S, Zheng F. Decadal variations of Pacific Walker circulation tied to tropical Atlantic-Pacific trans-basin SST gradients. *Environmental Research Letters* 2023, **18**(6): 064016.

74. Yao S-L, Wu R, Wang P, Chen S. Rapid high-latitude cooling in the southeastern Pacific

sector driven by North Atlantic warming during 1979–2013 in CESM1. *Environmental Research Letters* 2024, **19**(6): 064025.

75. Sathiyamoorthy V. Large scale reduction in the size of the tropical easterly jet. *Geophysical Research Letters* 2005, **32**(14).

76. Adam O, Bischoff T, Schneider T. Seasonal and interannual variations of the energy flux equator and ITCZ. Part I: Zonally averaged ITCZ position. *Journal of Climate* 2016, **29**(9): 3219-3230.

77. Donohoe A, Marshall J, Ferreira D, Armour K, McGee D. The interannual variability of tropical precipitation and interhemispheric energy transport. *Journal of Climate* 2014, **27**(9): 3377-3392.

78. Donohoe A, Marshall J, Ferreira D, McGee D. The relationship between ITCZ location and cross-equatorial atmospheric heat transport: From the seasonal cycle to the Last Glacial Maximum. *Journal of Climate* 2013, **26**(11): 3597-3618.

79. Frierson DM, Hwang Y-T. Extratropical influence on ITCZ shifts in slab ocean simulations of global warming. *Journal of Climate* 2012, **25**(2): 720-733.

80. Salzmann M, Cherian R. On the enhancement of the Indian summer monsoon drying by Pacific multidecadal variability during the latter half of the twentieth century. *Journal of Geophysical Research: Atmospheres* 2015, **120**(18): 9103-9118.

Figure legends

Fig. 1 | Two leading regimes of spring precipitation changes in inter-tropical Africa on inter-decadal timescales. **a**, Temporal evolutions of spring precipitation anomalies for 1950-2022 relative to the baseline period of 1981-2010 over inter-tropical Africa (12°S-12°N, 16°W-52°E demarcated by the purple box in **b** and **c**) from ERA5. The blue line denotes the original precipitation anomaly, and color bars indicate the reconstructed precipitation anomalies based on two leading modes of the empirical orthogonal function (EOF) analysis (see Methods). **b, c**, The first (**b**) and second (**c**) principal patterns are obtained by applying an EOF decomposition into the MAM-averaged precipitation anomalies for 1950-2022 over inter-tropical Africa (12°S-12°N, 16°W-52°E; excluding coastal or oceanic grids) and represent the tropical easterly jet (TEJ)-related and inter-tropical convergence zone (ITCZ)-related precipitation regimes, which explain 32.2% and 15.1% of the total variance, respectively. **d**, The standardized 9-year running-mean time series of the TEJ-related precipitation regime (color bars) and TEJ index (blue) from ERA5. **e**, The standardized 9-year rolling-mean time series of the ITCZ-related precipitation regime (color bars) and ITCZ index (blue) from ERA5 and the north-minus-south inter-hemispheric sea surface temperature (NH-SH SST) gradient index (red) from ERSST v3. The tropical SST mean (20°S-20°N) has been removed before calculating the NH-SH SST gradient index.

Fig. 2 | TEJ-dominated spring precipitation changes in inter-tropical Africa. **a**, Linear trends of the TEJ-related precipitation pattern for 1950-2022 based on the first EOF reconstruction alone (Fig. 1b, d; see Methods). **b**, Precipitation trends statistically linked to TEJ changes for 1950-2022. The TEJ-related precipitation trends are estimated by projecting the observed spring precipitation field onto the 9-year running mean spring TEJ time series (Methods). **c-d**, As in **b**, but for spring

vertical moisture advection trends (**c**) and 500-hPa pressure vertical velocity trends (**d**). **e**, Linear trends of moisture budget terms averaged over ITA (12°S-12°N, 16°W-52°E) for 1950-2022, including precipitation (P'), evaporation (E'), zonal moisture transport ($-\langle udq \rangle'$), meridional moisture transport ($-\langle vdq \rangle'$), vertical moisture transport ($-\langle \omega dq \rangle'$) and residual term (*residual'*). The precipitation minus evaporation ($P' - E'$) denotes the effective moisture. Vertical moisture advection comprises a thermodynamic component related to changes in atmospheric water vapor and a dynamic component caused by changes in atmospheric circulation (right two columns in **e**). **f**, Linear trends of spring vertical moisture advection during 1950-2022. **g**, As in **f**, but for spring 500-hPa vertical velocity trends. Stippling denotes regions where trends are statistically significant above the 95% confidence level, and error bars signify the 95% confidence interval based on a two-sided Student's *t*-test. Precipitation and atmospheric circulation data are derived from the ERA5 dataset.

Fig. 3 | ITCZ-mediated spring precipitation changes. **a-b**, spring precipitation (shading) and vertically integrated moisture flux (vector) (**a**), and surface temperature (**b**) are regressed against the 9-year running-mean time series of the ITCZ-related precipitation regime (color bars in Fig. 1e). **c-d**, Correlation coefficients of spring precipitation anomalies with the 9-year rolling-mean time series of ITCZ centroid index (**c**) and the north-minus-south inter-hemispheric SST gradient index (**d**), respectively. Surface temperature is from the NOAA merged land air temperature and ocean surface temperature. The north-south inter-hemispheric SST (NH-SH SST) gradient index from ERSST v3 is defined as the area-weighted SST difference between 30°N-60°N minus -30°S-0°. The tropical ocean (20S-20N) mean value has been removed to highlight the north-south inter-hemispheric warming contrast (**b**) before calculating the SST gradient index (**d**). Green lines (**a**

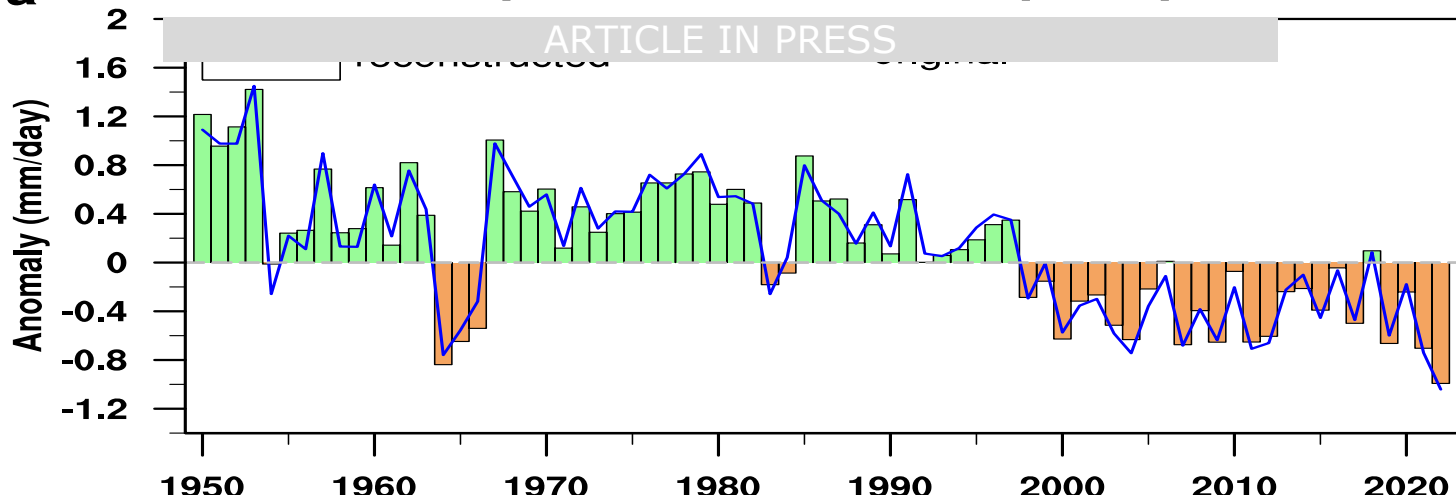
and **c-d**) denote the 6 mm/day contours of the climatological precipitation of 1981-2010. Stippling and vectors indicate regions where regression and correlation coefficients are statistically significant at the 95% confidence level based on a two-sided Student's *t*-test.

Fig. 4 | Constrained spring precipitation trends during 1950-2022 and for the near term (2026-2045) in ITA. **a-c**, Histograms of occurrence frequency of spring precipitation trends during 1950-2022 from 40 CESM1 runs (**a**), 100 MPI-ESM-LR runs (**b**), and 31 CMIP6 models (**c**) for original (orange) and adjusted (green) results accounting for the observed TEJ effect. Red (blue) dots represent the ensemble mean of trends with (without) the observed TEJ effect. Numbers signify the percentage of negative precipitation trends. **d**, Original (orange) and adjusted (green) trends for 1950-2022 are estimated from ERA5, observed TEJ-induced precipitation (Methods), as well as 8 CESM1 runs, 8 MPI-ESM-LR runs, and 8 CMIP6 models showing the largest strengthening of simulated TEJ decadal effect on precipitation. **e**, Trends during 2026-2045 under high-emission scenarios (RCP8.5 and SSP5-8.5). Light blue dots indicate the original trends, and pink dots denote the adjusted trends after removing the simulated TEJ effect. Error bars represent the 95% confidence interval based on a two-sided Student's *t*-test for observations and +/- 1SD of inter-member/inter-model precipitation trends for models. **f**, The fitted distributions of original (black) and adjusted (blue and red) precipitation trends for 2026-2045 from all models. Blue and red curves denote adjusted trends with the same amplitude as the observed TEJ due to a TEJ strengthening (-2SD per two decades) and weakening (+2SD per two decades), respectively. Black, blue, and red dots signify the ensemble mean of distributions with the corresponding colors. The green (brown) dashed line denotes the threshold of the probability of extreme wetting (drying) trends.

Inter-tropical African MAM precipitation

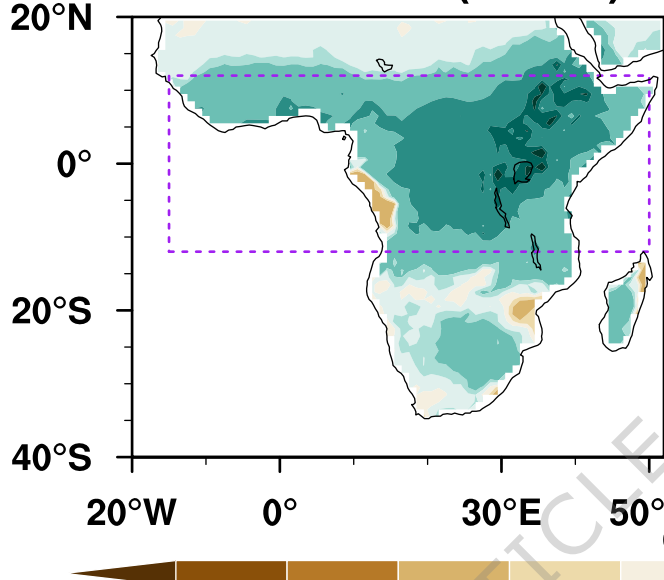
ARTICLE IN PRESS

a



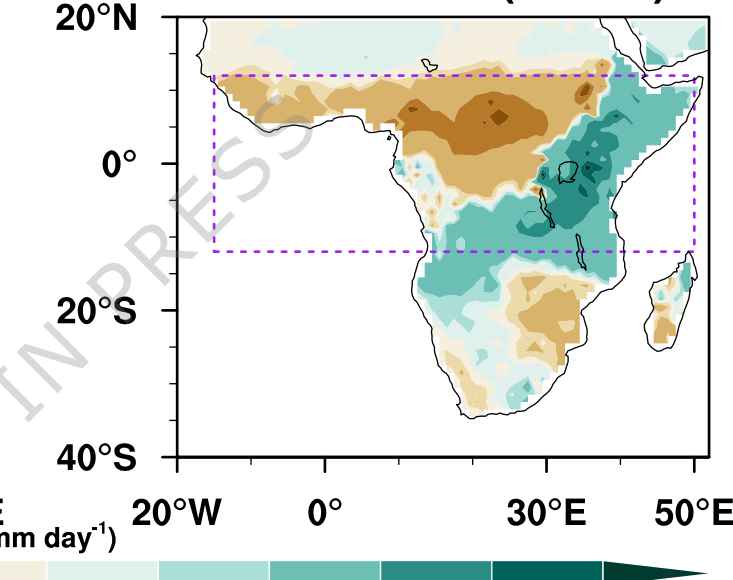
b

ERA5 EOF1 (32.2%)



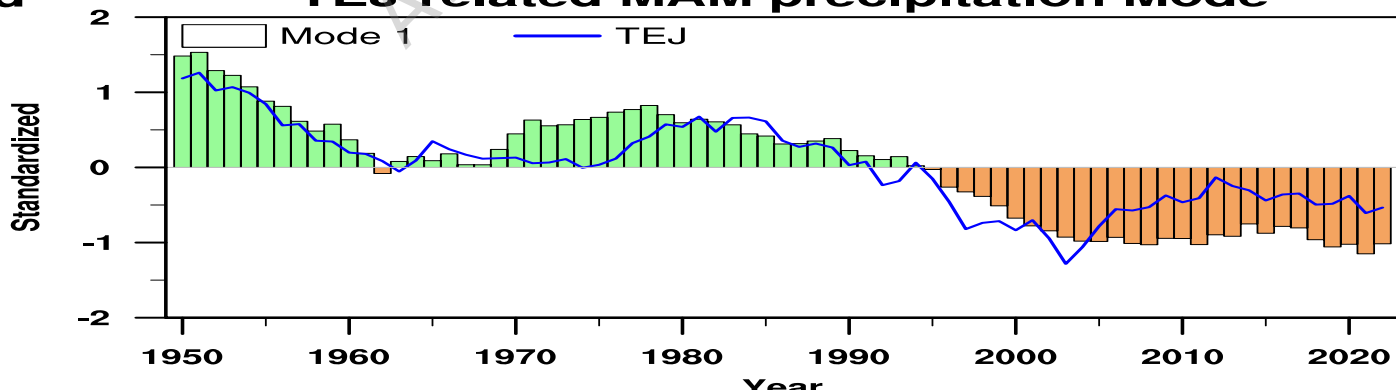
c

ERA5 EOF2 (15.1%)



d

TEJ-related MAM precipitation Mode



e

ITCZ-related MAM precipitation Mode

